Geophys. J. Int. (2004) **157,** 499–514 doi: 10.1111/j.1365-246X.2004.02209.x

The Kaiserslautern multiscale geopotential model SWITCH-03 from orbit perturbations of the satellite CHAMP and its comparison to the models EGM96, UCPH2002_02_0.5, EIGEN-1s and EIGEN-2

M. J. Fengler, W. Freeden and V. Michel

TU Kaiserslautern, Geomathematics Group, 67653 *Kaiserslautern,* PO Box 3049*, Germany. E-mail: freeden@mathematik.uni-kl.de*

Accepted 2003 November 25. Received 2003 November 11; in original form 2003 February 6

SUMMARY

Observed orbit perturbations of the near-Earth orbiting satellite CHAMP are analysed to recover the long-wavelength features of the Earth's gravitational potential. More precisely, by tracking the low-flying satellite CHAMP using the high-flying satellites of the Global Positioning System (GPS) the kinematic orbit of CHAMP is obtainable from GPS tracking observations, i.e. the ephemeris in Cartesian coordinates in an Earth-fixed coordinate frame (WGS84) becomes available.

In this study we are concerned with two tasks: first we present new methods for preprocessing, modelling and analysing the emerging tracking data. Then, in a first step we demonstrate the strength of our approach by applying it to simulated CHAMP orbit data. In a second step we present results obtained by operating on a data set derived from real CHAMP data.

The modelling is mainly based on a connection between non-bandlimited spherical splines and least-square adjustment techniques to take into account the non-sphericity of the trajectory. Furthermore, harmonic regularization wavelets for solving the underlying satellite-to-satellite tracking (SST) problem are used within the framework of multiscale recovery of the Earth's gravitational potential leading to SWITCH-03 (Spline and Wavelet Inverse Tikhonov regularized CHamp data). Further we show how regularization parameters can be adapted adequately to a specific region thereby improving a globally resolved model. Finally we compare the developed model with the EGM96 model, model UCPH2002_02_0.5 from the University of Copenhagen and the GFZ models EIGEN-1s and EIGEN-2.

Key words: CHAMP post-processed science orbit data, regional gravitational field recovery, spherical splines, Tikhonov wavelet regularization.

1 INTRODUCTION

Since the beginning of the space age, observed satellite orbit perturbations have been exploited to recover the long-wavelength features of the Earth's gravity field (see e.g. Barlier *et al.* 2000; Reigber *et al.* 1996, 2002, and references therein). Analysis of satellites' orbit perturbations are an essential tool for precise determination of the long-wavelength gravity field. Long-wavelength gravity models are of importance when studying deep-seated mass inhomogeneities and dynamics. In oceanography, long-wavelength geoid models give the reference surface for deriving the sea surface topography from altimetry, sea surface topography being a direct measure of the geostrophic flow (see e.g. Freeden & Hesse 2002).

The German Space Agency (DARA), the GeoForschungsZentrum (GFZ) and the German Aerospace Center (DLR) funded the CHAMP satellite mission (the satellite being launched in 2000), which was designed to bring about a breakthrough in long-to-mesoscale gravity field recovery by exploiting the near-polar orbit. Continuous coverage of the orbit data is provided by GPS satellite-to-satellite tracking data, while the non-gravitational orbit perturbations are directly measured by an onboard three-axis accelerometer. GFZ have performed numerical simulations in the spectral domain through an expansion of the gravitational potential in terms of spherical harmonics, taking into account suitable error models; these have proved that with CHAMP the accuracy of the gravity field model up to degree/order 30 can be improved by more than one decimal compared with the former models. Details of this globally oriented spherical harmonic modelling technique have been described several times in the literature (e.g. Reigber *et al.* 2002).

In this paper hi-lo SST (high–low satellite-to-satellite tracking) for the low Earth orbiter (LEO) CHAMP is discussed as proposed by Freeden (1999) from an alternative point of view. More precisely, hi-lo SST is understood as the problem of determining the external gravitational field of the Earth via a given set of gradient vectors

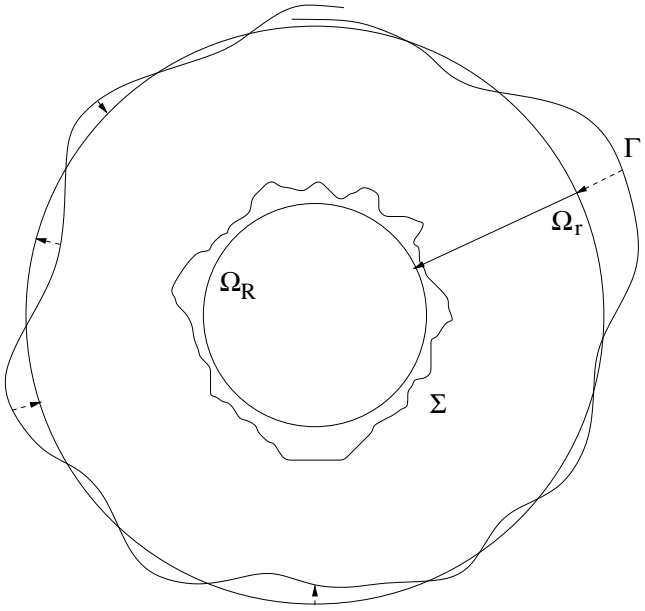

Figure 1. Illustration of the geometrical configuration.

at the altitude of CHAMP, which can be computed by numerically differentiating a kinematic orbit (see Section 2.2). In order to translate hi-lo SST into a mathematical formulation we start from the following geometrical situation (*cf.* Fig. 1).

Let the surface Σ of the Earth and the orbital set Γ of the LEO be given in such a way that Γ is a strict subset of the Earth's exterior Σ^{ext}. Further we denote by Ω_R a Bjerhammar sphere inside the Earth located at the origin of the Earth-fixed reference frame, and by Ω_r we denote a 'mean' orbit sphere going through the measurements.

Loosely speaking, the mathematical formulation of the hi-lo SST problem (see Freeden 1999) now reads as follows:

Let there be known the gradient vectors $v(x) = (\nabla V)(x)$, $x \in \Gamma$, for a subset $\Gamma \subset \Sigma^{ext}$ of points at the flight positions of the LEO. Find an approximation u of the geopotential field v on $\overline{\Sigma^{ext}}$, i.e. on and outside the Earth's surface, such that the difference of the geopotential field v and its approximation u is arbitrarily small on $\overline{\Sigma^{ext}}$ in terms of the underlying function spaces. In addition, the values $v(x)$, $x \in \Gamma$, should be consistent with the values $u(x)$, $\in \Gamma$.

The existence, uniqueness and well-posedness of the problem are discussed in Freeden *et al.* (2002). From the point of view of scientific computing the essential difficulties which must be overcome, are as follows:

(1) The data are error affected, i.e. we are confronted with the problem of operating on noisy CHAMP data. Hence, de-noising techniques have to be adapted to come closer to the 'real data set'.

(2) The data are given on a non-spherical orbit, thus 'downward continuation' is a much more difficult problem than in case of a spherical orbit. As a consequence the data must be transferred from the real orbit to a spherical reference orbit (see Fig. 1).

In what follows, both problems will be investigated intensively from a numerical point of view. In particular we are interested in getting regional and locally improved models from real (de-noised) CHAMP data sets. The latter case in particular will demonstrate the strength of our wavelet method, since local adaptation of regularization parameters is much easier than using spherical harmonic expansions because of their non-space localizing character. Instead we are concerned with locally oriented regularization by virtue of multiresolution analysis using adequately constructed wavelets. These concepts will be introduced in Sections 2.4.2 and 2.5.

2 PRELIMINARIES

In order to translate the satellite-to-satellite tracking problem as required for the CHAMP mission into a mathematical formulation we need some mathematical pre-requisites that should be explained now:

Each point of the three-dimensional Euclidean space $\mathbb{R}^3$, $x = (x_1, x_2, x_3)^{\mathrm{T}}$, $|x| \neq 0$, allows a unique representation of the form $x = r\xi$, $r = |x|$, $\xi = (\xi_1, \xi_2, \xi_3)^{\mathrm{T}}$, where $\xi \in \mathbb{R}^3$, $|\xi| = 1$, is the uniquely determined directional unit vector of $x \in \mathbb{R}^3$. Throughout this work we may regard this coordinate system as the usual Earth-fixed reference frame in which the CHAMP ephemerides are given, e.g. WGS84. The sphere in $\mathbb{R}^3$ with radius r around the origin is denoted by Ω_r, i.e. $\Omega_r = \{x \in \mathbb{R}^3 | |x| = r\}$. For later use we reserve the notation Ω_R to denote the Bjerhammar sphere inside the Earth (see Fig. 1). With Ω_r^{ext} we denote the exterior of Ω_r, while Ω_r^{int} is the interior of Ω_r. By definition, we let Ω be the unit sphere Ω_1, if no confusion is likely to arise.

As usual, we introduce the spherical harmonics as restrictions of homogeneous harmonic polynomials to Ω. To be specific, let $H_n : \mathbb{R}^3 \to \mathbb{R}$ be a homogeneous harmonic polynomial of degree n, then the restriction $Y_n = H_n|_\Omega$ is called a *spherical harmonic of degree n*. The space of all spherical harmonics of degree n is denoted by $\mathrm{Harm}_n(\Omega)$, and its dimension $\dim(\mathrm{Harm}_n(\Omega))$ is known to be $2n + 1$, see Müller (1966). Further we mean by $\mathrm{Harm}_{p,\ldots,q}(\Omega)$ the space of all spherical harmonics from degree p up to q. Spherical harmonics of different degrees are orthogonal in the sense of the $\mathcal{L}^2(\Omega)$-inner product

$$(Y_n, Y_m)_{\mathcal{L}^2(\Omega)} = \int_\Omega Y_n(\xi) Y_m(\xi)\, d\omega(\xi) = 0, \quad n \neq m,$$

where $d\omega$ is the surface element on Ω. Any spherical harmonic Y_n, $n \in \mathbb{N}_0$, is an infinitely often differentiable eigenfunction of the Beltrami operator Δ^* corresponding to the eigenvalue $(\Delta^*)\hat{}(n)$, $n \in \mathbb{N}_0$:

$$\Delta_\xi^* Y_n(\xi) = (\Delta^*)\hat{}(n) Y_n(\xi), \quad \xi \in \Omega, \quad Y_n \in \mathrm{Harm}_n(\Omega),$$

where the *spherical symbol* $\{(\Delta^*)\hat{}(n)\}_{n\in\mathbb{N}_0}$ of the operator Δ^* is given by $(\Delta^*)\hat{}(n) = -n(n+1)$, $n = 0, 1, \ldots$, Separating the longitude-independent part of the Beltrami operator yields the Legendre operator $L_t = (\frac{d}{dt})(1 - t^2)(\frac{d}{dt})$. The well-known *Legendre polynomials* $P_n : [-1, +1] \to \mathbb{R}$ *of degree n* are defined as the infinitely often differentiable eigenfunctions of the Legendre operator L_t corresponding to the eigenvalue $-n(n+1)$, which are bounded for $t = 1$ and satisfy $P_n(1) = 1, n \in \mathbb{N}_0$. They form an orthogonal system with respect to the $\mathrm{L}^2([-1, +1])$-inner product. A connection between the spherical harmonics $\{Y_{n,k}\}_{k=-n,\ldots,n}$ and the Legendre polynomials is provided by the well-known addition theorem, which will turn out to be the essential key for the whole method presented in this paper (e.g. Freeden *et al.* 1998). For later use we introduce here $Y_{n,k}^R = \frac{1}{R} Y_{n,k}$.

2.1 Spherical grids

The literature contains a variety of adequate lattices used for numerical integration to determine integral expressions for a continuous function V on the sphere, such that

$$\int_\Omega V(x)\, d\omega(x) \approx \sum_{i=0}^{M} \omega_i V(x_i).$$

Most common techniques profit by discretization from an equidistribution of the used lattice leading to low-discrepancy methods, e.g. the Reuter or Brandt grid (see, e.g. Freeden *et al.* 1998). But for a spherical harmonic exact integration formula (see e.g. Freeden 1999) one has to determine the integration weights even for moderate point systems by solving highly ill-conditioned linear systems. Thus, for simplicity, we are led to use for approximate integration an equiangular longitude–latitude grid, as discussed, for example, by Driscoll & Healy (1994).

In our approach an equidistributed grid, due to Reuter (1982), is of particular importance for the data selection strategy.

Definition 2.1 (Reuter grid)

A pointset $X_{N(\gamma)}$, called the *Reuter grid* on the unit sphere and dependent on the choice of a control parameter $\gamma \in \mathbb{N}$, is given by the points (ϕ_{ij}, θ_i) as follows:

(i) $\theta_0 = 0, \phi_{01} = 0$ (North Pole)
(ii) $\Delta\theta = \pi/\gamma$
(iii) $\theta_i = i\Delta\theta, 1 \le i \le \gamma - 1$
(iv) $\gamma_i = 2\pi / \arccos[(\cos\Delta\theta - \cos^2\theta_i)/\sin^2\theta_i]$
(v) $\phi_{ij} = (j - \frac{1}{2})(2\pi/\gamma_i), 1 \le j \le \gamma_i$
(vi) $\theta_\gamma = \pi, \phi_{\gamma 1} = 0$ (South Pole).

2.2 Numerical differentiation

As pointed out in our introduction, by modelling the acceleration, i.e. the gradient (∇V) of the gravitational potential V, we are confronted with determination of the second-order derivative numerically from discrete (noisy) CHAMP ephemeris. As is well-known, numerical differentiation is an ill-posed problem in the sense of Hadamard's definition, e.g. the uniqueness cannot usually be assured. Nevertheless, there do exist algorithms and methods including error estimates to solve the underlying problem: for some theoretical issues see Ahlberg *et al.* (1967), Engeln-Müllges & Reutter (1988), Press *et al.* (1992), Werner (1992) and Schwarz (1997) and with application to satellite missions Austen & Reubelt (2000), Grafarend & Shen (2000), Glockner (2001) and Reubelt *et al.* (2003).

Since numerical differentiation techniques are well known we present only two methods which proved to have good behaviour in practice and which can be recommended for future work in hi-lo SST (*cf.* Fengler 2002; Reubelt *et al.* 2003).

The first technique is based on Newton interpolation and gives us the so-called Newton–Gregory method (*cf.* Engeln-Müllges & Reutter 1988; Grafarend & Shen 2000). For our purpose the methods for determining the second derivative are of special interest, and can be written down for seven and nine adjacent time-steps t_i as listed below:

$$
\begin{aligned}
f''(t_i) \approx \frac{1}{h^2}\Big(&\frac{1}{90}f(t_{i-3}) - \frac{3}{20}f(t_{i-2}) + \frac{3}{2}f(t_{i-1}) \\
&- \frac{49}{18}f(t_i) + \frac{3}{2}f(t_{i+1}) - \frac{3}{20}f(t_{i+2}) + \frac{1}{90}f(t_{i+3})\Big) \\
f''(t_i) \approx \frac{1}{h^2}\Big(&-\frac{1}{560}f(t_{i-4}) + \frac{8}{315}f(t_{i-3}) - \frac{1}{5}f(t_{i-2}) \\
&+ \frac{8}{5}f(t_{i-1}) - \frac{205}{72}f(t_i) + \frac{8}{5}f(t_{i+1}) - \frac{1}{5}f(t_{i+2}) \\
&+ \frac{8}{315}f(t_{i+3}) - \frac{1}{560}f(t_{i+4})\Big). \qquad (1)
\end{aligned}
$$

2.2.1 *Spline differentiation techniques*

Due to numerical round-off errors that usually occur with increasing polynomial degree of the underlying Newton interpolation formula, it also seems to be reasonable to consider an approximating spline approach as explained in Engeln-Müllges & Reutter (1988). A detailed algorithmic formulation to determine the spline coefficients from a band-diagonal matrix formulation can be found in Fengler (2002) and is omitted here.

In this context it should be mentioned that a good *a priori* choice for the weights in practice depends greatly on knowledge about the underlying noise model. However, there do exist several alternative strategies to find appropriate weights (e.g. cross-validation Kusche 2002; Green & Silvermann 1994).

For numerical differentiation one computes in a first step an approximating natural cubic spline through the data, getting immediately two different possibilities for continuing:

(1) Calculate analytically the first- and second-order derivative of the spline at the orbit positions. We call this spline differentiation (SPD).

(2) Calculate analytically the first-order derivative in the orbit positions and fit another natural cubic spline through these first-order derivatives. Afterwards calculate from this spline the first-order derivative analytically and thus one gets an approximation to the second-order derivative of the initial problem. This is called spline-on-spline differentiation (SPS).

As it is shown in Ahlberg *et al.* (1967) and with application to the ephemeris in Fengler (2002) the SPS concept beats SPD with respect to accuracy, especially on noisy data. Beyond this, it is shown in Fengler (2002) that with application to noise-free simulated CHAMP ephemerides the error induced by the numerical differentiation SPS scheme is of the same order as the seven- and nine-point Newton–Gregory formulae.

2.3 Noise model

To demonstrate the efficiency of our later formulated method it is necessary to simulate a realistic noise model and test additionally corresponding de-noising methods. Grafarend & Shen (2000) presented a noise model study and proposed an autoregressive (AR(1)) process producing a small but highly correlated noise for adjacent ephemerides. This model assumes that measurements in a certain spatial and time interval are mostly effected by the *same* noise sources, e.g. a highly correlated noise originating from the GPS measurements.

Remark 2.1 (Noise model)

Let ε_t be Gaussian (strictly stationary) white noise, with variance σ_ε^2. Then the sequence of random variables X_t of an AR(1) process is given by $X_t = \alpha\, X_{t-1} + \varepsilon_t$. There exists for $|\alpha| < 1$ a unique stationary solution to the AR(1) process. Further we know that $EX_t = 0$, $\mathrm{var}X_t = \frac{\sigma_\varepsilon^2}{1-\alpha^2}$, $r_t = \sigma_\varepsilon^2 \frac{\alpha^{|t|}}{1-\alpha^2}$ and $\rho_t = \alpha^{|t|}$, where r_t denotes the autocovariance and ρ_t the autocorrelation function (*cf.* Stockis 2001). In other words, we are able to conclude that high correlations are induced for α close to 1.

In Austen & Reubelt (2000) and Reubelt *et al.* (2003) it is shown that the Newton–Gregory formulae are able to significantly reduce measurement errors due to their formulation by coordinate differences. The AR(1) process itself inherits its autocorrelation function to the coordinate differences. In practice great importance lies in removing a bias.

By determining a smoothing factor via cross-validation of the numerical differentiation with approximating splines one can achieve the same error order (or more details see Fengler 2002).

Gravitational forces acting on the satellite should also be modelled, e.g. gravitational forces induced by the Moon and Sun, but

also non-gravitational forces, e.g. those induced by solar pressure, air drag etc. This has been neglected since the 'real data' are assumed to be pre-processed with regard to those conservative and non-conservative effects, e.g. by using the accelerometer on board CHAMP (see Reigber *et al.* 1996, 2002).

2.3.1 De-noising methods

In our concept of modelling the emerging tracking data we have to apply numerical differentiation to evaluate the radial derivative. Since the aforementioned concepts of numerical differentiation are both linear in the observations, we apply the de-noising step after having differentiated. Both methods profit essentially from a formulation of coordinate differences, so that in practice they are able to remove biases.

To remove the noise from the data we use translation-invariant wavelet de-noising (TI de-noising) (see Daubechies 1988; Sweldens & Jawerth 1994). Hard and soft thresholding with application to simulated ephemerides have also been studied, but they turned out to be worse (compare the results in Fengler 2002). A detailed introduction to these de-noising concepts can be found in Mallat (1999). Coifman & Donoho (1995) show that TI de-noising has decorrelating properties and can significantly reduce the noise-containing wavelet coefficients if there is an *a priori* known error distribution.

As an alternative approach we studied cubic smoothing splines, where we determined a global smoothing parameter by cross-validation (*cf.* Fengler 2002; Kusche 2002; Green & Silvermann 1994).

Now let us recapitulate the concept of (least-square) $\mathcal{H}$-splines, which in geophysics is also known as least-square collocation (Moritz 1980). These $\mathcal{H}$-splines allow us to take into account the non-sphericity of the geometry of the orbit. Thus, the main motivation for using $\mathcal{H}$-splines within our method lies in extrapolating the measurements to a mean orbital sphere, see Fig. 1.

2.4 $\mathcal{H}$-splines

The following definitions and theorems including proofs are mainly based on results which can be found in Freeden (1981a, 1999) and Glockner (2001) and references therein. A reproducing kernel structure on the underlying Hilbert space is essential for constructing spherical splines:

Definition 2.2 The reproducing kernel

Let $D \subset \mathbb{R}^n$ and $\mathcal{H}$ be a Hilbert space of functions $F : D \to \mathbb{R}$, equipped with the inner product $(\cdot, \cdot)_{\mathcal{H}}$. Then a function $K_{\mathcal{H}}(\cdot, \cdot)$ of two variables in D is called the reproducing kernel function for the space $\mathcal{H}$, if

(i) for each fixed $x \in D$, $K_{\mathcal{H}}(x, \cdot)$ and $K_{\mathcal{H}}(\cdot, x)$ are members of $\mathcal{H}$,

(ii) for every $F \in \mathcal{H}$ and for every $x \in D$, the reproducing property

$$F(x) = (F, K_{\mathcal{H}}(x, \cdot))_{\mathcal{H}}$$

holds.

The definition of $\mathcal{H}$-splines reads as follows:

Definition 2.3 $\mathcal{H}$-spline

Suppose that $\mathcal{L}_1, \ldots, \mathcal{L}_N$ is a set of linearly independent bounded linear functionals on a reproducing kernel Hilbert space $\mathcal{H}(\overline{\Omega_R^{\text{ext}}})$, which we denote briefly by $\mathcal{H}$, with reproducing kernel $\mathcal{K}_{\mathcal{H}}(\cdot, \cdot)$. Then we call any function of the form

$$S(x) = \sum_{i=1}^{N} a_i \mathcal{L}_i \mathcal{K}_{\mathcal{H}}(\cdot, x), \quad x \in \overline{\Omega_R^{\text{ext}}},$$

an $\mathcal{H}$-spline relative to the system $\mathcal{L}_1, \ldots, \mathcal{L}_N$. The space of all $\mathcal{H}$-splines relative to $\mathcal{L}_1, \ldots, \mathcal{L}_N$ is an N-dimensional linear subspace of $\mathcal{H}$ and is briefly denoted by $\mathcal{S}_{\mathcal{H}}(\mathcal{L}_1, \ldots, \mathcal{L}_N)$.

In the following we state briefly the most important result derived for $\mathcal{H}$-splines, (*cf.* Freeden 1981a, 1983; Freeden *et al.* 1997).

Theorem 2.1 *Suppose that $F \in \mathcal{H}$. The spline interpolation problem*

$$\left\| S^F_{\mathcal{L}_1,\ldots,\mathcal{L}_N} \right\|_{\mathcal{H}} = \inf_{\substack{H \in \mathcal{H} \\ \mathcal{L}_i H = \mathcal{L}_i F, i=1,\ldots,N}} \|H\|_{\mathcal{H}}$$

is well-posed in the sense that its solution exists, is unique, and depends continuously on the data $\mathcal{L}_i F, i = 1, \ldots, N$. The uniquely determined solution is given in the explicit form

$$S^F_{\mathcal{L}_1,\ldots,\mathcal{L}_N}(x) = \sum_{i=1}^{N} a_i^N \mathcal{L}_i K_{\mathcal{H}}(\cdot, x), \quad x \in \overline{\Omega_R^{\text{ext}}},$$

where the coefficients $a_1^N, \ldots, a_N^N$ satisfy the linear equations:

$$\sum_{j=1}^{N} a_j^N \mathcal{L}_i \mathcal{L}_j K_{\mathcal{H}}(\cdot, \cdot) = \mathcal{L}_i F, \quad i = 1, \ldots, N.$$

By focusing on Sobolev spaces and pseudodifferential operators (PDO) in Sections 2.4.2 and 2.4.3 we are led to certain criteria for choosing the reproducing kernel and the linear functionals.

2.4.1 Least-squares adjustment

Motivated by the theory of $\mathcal{H}$-splines we can view certain reproducing kernels from another very practical point of view: we may regard the $\mathcal{H}$-spline just as a special function of two variables, and in connection with the addition theorem of spherical harmonics shaped most commonly on a sphere as a symmetric *hat*. Further, applying $\mathcal{H}$-spline interpolation requires us to solve a linear system, whose size increases quadratically with increasing number of measurements. We assume that we have a kinematic orbit of 10 days from CHAMP, which implies a good 'first coverage' of the Earth by providing us a (position) measurement every 30th second. Then we have to solve a linear system of about $28\,800^2$ elements. Reasonable methods exist for carrying out this task, e.g. starting from storing only the upper part of the matrix and ending in fast multipole methods or domain decomposition methods (Glockner 2001; Michel 2001; Gutting 2002). The essential task is that one has to find a spline coefficient via a large and (usually) highly ill-conditioned system for each point of the measurement.

In the case of noisy data smoothing (regularization) parameters have to be found, and probably the system has to be solved more than once. Additionally, if we consider satellite missions concerned with gravity field evaluation we *a priori* know that these missions only have a *physically relevant precision* up to a certain degree, e.g. the spherical harmonic degree. For CHAMP, for example, the precision of the missions with respect to gravitational field recovery is said to be at least degree 90 up to degree 120 (*cf.* Reigber *et al.* 1996).

Thinking about the expansion in terms of outer harmonics it is obvious that we would need only a system with a small selection of the 10-day orbit for about $121^2 = 14\,641$ unknowns to fit a solution. But then we omit the information which is probably somehow contained in the remaining data.

The point of departure in our approach is a least-squares adjustment procedure as proposed in the following.

Definition 2.4 (Least-squares adjustment)

Denoting by $\mathcal{K}_{\mathcal{H}}(\cdot,\cdot)$ a reproducing kernel, by $P=\{y_j, j=1,\dots,N|y_j\in\Omega_R\}$ a (fundamental) system locating the kernels, and by $M=\{x_j, j=1,\dots,M|x_j\in\Gamma\}$ the set of measurement positions, we find with $\widetilde{S}$ by

$$\widetilde{S}(x)=\sum_{j=1}^{N}a_j^N\mathcal{K}_{\mathcal{H}}(x,y_j),\quad x\in\overline{\Omega_R^{\text{ext}}},$$

a (discrete) least-squares approximation to the measurements F_i, $i=1,\dots,M$ at the measuring positions where the coefficients a_j^N are the least-squares solution of the overdetermined (i.e. $M>N$) linear system defined by

$$\sum_{j=1}^{N}a_j^N\mathcal{K}_{\mathcal{H}}(x_i,y_j)=F_i,\quad i=1,\dots,M.$$

The set P is later called a *park grid* due to the fact that it refers the kernels to particular locations.

Remark 2.2

P is a fundamental system if and only if it provides the full column rank of the linear system (*cf.* Freeden 1999). Good choices of P minimize the condition number and take care of a physically relevant distribution of the located kernels (for example, the Reuter grid as stated in Definition 2.1).

2.4.2 *Sobolev spaces*

For our modelling we need some more specified tools which are well-known from the theory of Sobolev spaces (see Freeden 1981b; Freeden 1999).

Definition 2.5

Let A be a PDO with the singular value decomposition $AY_{n,k}=A^{\wedge}(n)Y_{n,k}; n\in\mathbb{N}_0, k\in\{-n,\dots,n\}$, i.e. A is isotropic and we briefly write $A_n=A^{\wedge}(n)$.

The Sobolev space $\mathcal{H}(A,\Omega_R)$ is defined by

$$\mathcal{H}(A,\Omega_R)=\overline{\left\{F\in C^{(\infty)}(\Omega_R)|AF\in \mathrm{L}^2(\Omega_R)\right\}}^{\|\cdot\|_{\mathcal{H}(A,\Omega_R)}}$$
$$=\overline{\left\{F\in C^{(\infty)}(\Omega_R)\left|\sum_{n=0}^{\infty}\sum_{k=-n}^{n}A_n^2\left(F,Y_{n,k}^R\right)^2_{\mathrm{L}^2(\Omega_R)}<\infty\right.\right\}}^{\|\cdot\|_{\mathcal{H}(A,\Omega_R)}},$$

where we let $\|F\|_{\mathcal{H}(A,\Omega_R)}=\|AF\|_{\mathrm{L}^2(\Omega_R)}$. Obviously $\mathcal{H}(A,\Omega_R)$ equipped with the inner product $(F,G)_{\mathcal{H}(A,\Omega_R)}=(AF,AG)_{\mathrm{L}^2(\Omega_R)}$ is a separable Hilbert space.

The Abel–Poisson kernel is the uniquely determined reproducing kernel of the Sobolev space $\mathcal{H}(A,\Omega_R)$ with symbol $A_n=h^{-n/2}, n\in\mathbb{N}_0, 0<h<1$. We use this kernel in our computation for the following reasons: first, the rotational invariance of the kernel (spherical radial basis function) allows us to shift the maximum (the 'hat') to the knots given by the park grid. Second, the parameter h controls the width of the hat in the sense of a dilation of the kernel, which corresponds to a frequency modulation due to the uncertainty principle (see Freeden & Michel 1999). Moreover, we assume the Abel–Poisson kernel to be physically relevant by identifying it with the *downward continuation* operator. For many other kernels, e.g. the singularity kernel, we refer to Freeden *et al.* (1997) and the considerations therein.

Some nice numerical properties of the Abel–Poisson kernel should be outlined: one bonus for an ease of computation is that the Abel–Poisson kernel possesses an elementary representation given as

$$K_{\mathcal{H}(A,\Omega_R)}(x,y)=\sum_{n=0}^{\infty}\frac{2n+1}{4\pi R^2}h^nP_n\left(\frac{x}{|x|}\cdot\frac{y}{|y|}\right)=\frac{1}{4\pi R^2}\frac{1-h^2}{(L_h(x,y))^{3/2}}\tag{2}$$

with

$$L_h(x,y)=1+h^2-2h(x\cdot y).$$

Of course, this has the advantage that an infinite series need not to be evaluated by summation. But this point should be further outlined from a computational point of view: using any non-elementary representation, e.g. even bandlimited kernels such as the Shannon or cubic polynomial (CuP) kernel (see Freeden *et al.* 1998), results in a very expensive computational effort which must be avoided. Although fast algorithms exist for evaluating the Legendre polynomials the time required for the matrix initialization dominates the solution process.

Another advantage of stabilizing the linear systems is the symmetry, positivity and smoothness of the Abel–Poisson kernel, which can easily be controlled by the parameter h, in particular on a spherical shell (see Fig. 2). It is a task for the future to find out under what circumstances the spline matrix is best conditioned by changing to different *physically relevant* kernels under fixing the point set.

Moreover, Glockner (2001) and Michel (2001) have developed highly efficient algorithms for solving spline systems induced by single poles in linear amounts using fast multipole methods. Finally, we want to make the spline approach more concrete with respect to computational aspects by choosing the evaluation functional as a bounded linear functional.

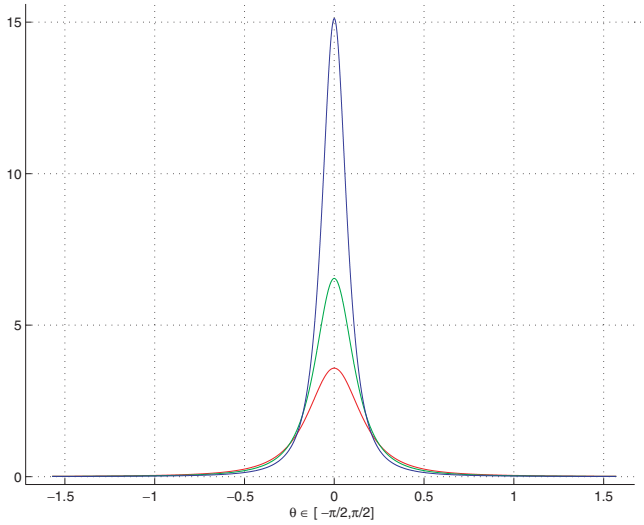

Figure 2. Sectional representation of the Abel–Poisson scaling function on Ω with $h\in\{0.8, 0.85, 0.9\}$.

2.4.3 *SST operator*

Observing the results above we can extend the introduced PDO concept involving the (negative) first radial derivative of a function $V\in\mathcal{H}(A,\Omega_R)$ to the outer space at height $r>R$, by connecting it with the upward continuation operator (for more details see Freeden 1999). More explicitly, we have

$$-x\cdot(\nabla_x V)(x)=\sum_{n=0}^{\infty}\sum_{k=-n}^{n}V^{\wedge}(n,k)(n+1)\left(\frac{R}{|x|}\right)^{n+1}\frac{1}{A_n}Y_{n,k}^R,\tag{3}$$

for all $x \in \Omega_R^{\text{ext}}$. The SST operator for the CHAMP mission

$$\Lambda_{\text{SST}} : \mathcal{H}\big(A, \overline{\Omega_R^{\text{ext}}}\big) \to \mathcal{H}\big(\Lambda_{\text{SST}}^{-1}A, \overline{\Omega_r^{\text{ext}}}\big),$$
$$x \mapsto \Lambda_{\text{SST}}(V)(x) = -x \cdot (\nabla_x V)(x),$$

can be interpreted as a PDO defined on $\mathcal{H}(A, \overline{\Omega_R^{\text{ext}}})$ with the symbol

$$(\Lambda_{\text{SST}})^\wedge(n) = (n+1)\left(\frac{R}{r}\right)^{n+1}. \tag{4}$$

As the reader has probably noticed, we did not really introduce the radial derivative formally given by the operator $\frac{x}{|x|} \cdot \nabla_x$ but the expression $x \cdot \nabla_x$. The obvious reason for this (see Freeden 1999) is that by neglecting the denominator we enforce harmonicity of the 'radial' derivative, which is very important for our approach later on where we use the Abel–Poisson splines as harmonic functions for approximating the data (*cf.* Fengler 2002). Therefore, when we speak in what follows of the radial derivative, we in fact mean $x \mapsto x \cdot \nabla_x V(x)$, $x \in \Omega_R^{\text{ext}}$.

2.5 Tikhonov regularization wavelets

Next we deal with the solution of the SST problem based on the operator defined by (4). If no confusion is likely to arise we denote Λ_{SST} simply by $\Lambda : \mathcal{H}(\overline{\Omega_R^{\text{ext}}}) \to \mathcal{H}(\overline{\Omega_r^{\text{ext}}})$,

$$\Lambda V = G, \quad V \in \mathrm{L}^2(\Omega_R), \quad G \in \mathrm{L}^2(\Omega_r).$$

As we know from the literature (*cf.* Freeden 1999; Glockner 2001), the latter equation is an exponentially ill-posed pseudodifferential equation with an unbounded inverse operator Λ^{-1}. The idea of regularization is now to replace the inverse operator by another more suitable operator to approximate the solution. By operating directly on the singular values of Λ^{-1}, wavelets turn out to be a very appropriate tool for solving the underlying inverse problem.

Definition 2.6

A family of linear operators $S_j : \mathcal{H}(\overline{\Omega_r^{\text{ext}}}) \to \mathcal{H}(\overline{\Omega_R^{\text{ext}}})$, $j \in \mathbb{N}_0$, is called a *regularization* of Λ^{-1}, if it satisfies the following properties:

(i) S_j is bounded on $\mathcal{H}(\overline{\Omega_r^{\text{ext}}})$ for all $j \in \mathbb{N}_0$,
(ii) for any member $G \in \text{im}(\Lambda)$, the limit relation

$$\lim_{j\to\infty} S_j G = \Lambda^{-1} G$$

holds in $\|\cdot\|_{\mathcal{H}(\overline{\Omega_R^{\text{ext}}})}$ topology.

Since we are only interested in the potential values on Ω_R we can reduce the bilinear case (as given in Freeden *et al.* 1999) to a linear wavelet approach. Thus, we obtain the J-level regularization of the potential V on Ω_R by evaluating the convolution $V_J = \Phi_J * G = \int_{\Omega_r} \Phi_J(\cdot,\eta)G(\eta)\,d\omega_r(\eta)$, where Φ_J denotes the J-level regularization and reconstruction Tikhonov scaling function. This scaling function is defined as follows:

Definition 2.7

For a given decreasing positive sequence $\gamma_j, j \in \mathbb{N}_0$ with $\lim_{j\to\infty}\gamma_j = 0$, the SST Tikhonov regularization scaling function is defined by

$$\Phi_j(x,y) = \sum_{n=0}^{\infty} \phi_j(n)\frac{2n+1}{4\pi Rr}\left(\frac{Rr}{|x||y|}\right)^{n+1} P_n\left(\frac{x}{|x|}\cdot\frac{y}{|y|}\right),$$

for all $x \in \Omega_R$, $y \in \Omega_r$, where the symbol $\phi_j(n)$ is given by

$$\phi_j(n) = \frac{\Lambda^\wedge(n)}{(\Lambda^\wedge(n))^2 + \gamma_j}, \quad n = 0, 1, \ldots; j \in \mathbb{N}_0,$$

corresponding to the singular values

$$\Lambda^\wedge(n) = (n+1)\left(\frac{R}{r}\right)^{n+1}.$$

Due to the decreasing symbol for large n, we may regard these functions as low-pass filters similar to Tikhonov regularization as known for ill-conditioned linear systems. The SST Tikhonov regularization wavelets are analogously obtained as bandpass filters, i.e. by the difference of two subsequent low-pass filters (see Freeden 1999):

Definition 2.8

For a given decreasing sequence γ_j, $j \in \mathbb{N}_0$ of positive values we define the SST regularization wavelet by

$$\Psi_j(x,y) = \sum_{n=0}^{\infty} \psi_j(n)\frac{2n+1}{4\pi Rr}\left(\frac{Rr}{|x||y|}\right)^{n+1} P_n\left(\frac{x}{|x|}\cdot\frac{y}{|y|}\right),$$

for all $x \in \Omega_R$, $y \in \Omega_r$, where the symbol $\psi_j(n)$ is given by

$$\psi_j(n) = \phi_{j+1}(n) - \phi_j(n), \quad n = 0, 1, \ldots; j \in \mathbb{N}_0.$$

Thus, we obtain the J-level detail (bandpass) level of the potential V on Ω_R by evaluating the convolution $\Psi_J * G = \int_{\Omega_r} \Psi_J(\cdot,\eta)G(\eta)\,d\omega_r(\eta)$. This convolution is also called the *linear wavelet transformation*.

3 MODELLING OF THE CHAMP MISSION

3.1 Simulation

Since CHAMP is tracked by the GPS we can assume that its (discrete) ephemeris $E = \{(t_i, x_{ei}), i = 1, \ldots, N : t_i \in \mathbb{R}, x_{ei} \in \Gamma\}$, where $\Gamma \subset \Sigma^{\text{ext}}$ as illustrated in Fig. 1, is describable in an Earth-fixed reference frame with the origin centred at the centre of gravity of the Earth, with the z-axis pointing along the axis of rotation ('North Pole'), and the x-axis towards the intersection point of the equator and the zero meridian (Greenwich) at longitude 0°. In our simulations we neglected nutation and precession of the Earth. With the program MOVSAT from Balmino & Barriot (1989) we simulated a 90-day orbit of CHAMP based on an EGM96 gravity field model up to degree 200 sampled every 10th of a second. We used CHAMP's Kepler elements provided by the GFZ for the launch as the initial start configuration (*cf.* Reigber *et al.* 1996). For the prediction from the equation of motion MOVSAT uses the Adams–Moulton–Cowell method, which is a multistep predictor-corrector method. This program is well known and has been tested over more than 20 yr of use: for example, see other publications in a similar context by Glockner (2001) and Kusche (2002). We added to each Cartesian component independently the noise generated from the introduced model of Section 2.3 with $\alpha = 0.8$ and a standard deviation of $\sigma_\varepsilon = 1$ m (see the proposed example by Grafarend & Shen 2000). This produces highly correlated perturbations in the simulated trajectory of ±1.7 m. This seems to be a realistic noise with respect to all other error sources, e.g. errors in GPS measurements, accelerometer drifts, non-modelled third-body forces etc. (see also Grafarend & Shen 2000; Reigber *et al.* 1996).

3.2 Pre-processing

For the evaluation of the gradient (∇V) of the potential we transform the ephemeris E into a quasi-inertial system of CHAMP. The set E

then becomes the so-called space-fixed ephemeris $S = \{(t_i, x_{si}), i = 1, \ldots, N : t_i \in \mathbb{R}, x_{si} \in \Omega_R^{\text{ext}}\}$, where $x_{s\text{i}}$ denotes the locations in the inertial frame.

In our model the transformation is explicitly done by applying an orthogonal transformation matrix $R(t)$ to the ephemeris. $R(t)$ depends here on the *fixed* angular velocity ω of the Earth, which is given via the siderial time and an initial angular configuration depending of the Julian date t (*cf.* Austen & Reubelt 2000; Grafarend & Shen 2000).

By numerically differentiating the elements of S twice with respect to t given by (1) or SPS and applying Newton's law of inertial motion we determine the gradient (∇V) (*cf.* Fengler 2002; Grafarend & Shen 2000; Reubelt *et al.* 2003).

Equipped with the gradient we are able to determine the radial derivative in the Earth-fixed coordinate system by the relation from the inertial system:

$$\frac{x_s}{|x_s|} \cdot (\nabla V)(x_s) = \frac{x_s}{|x_s|} \cdot \ddot{x}_s = \frac{\partial}{\partial r} V(x_e),$$

where $x_e = r \cdot \xi$, with $r = |x_e|$.

When dealing with real data it is of essential importance to apply after the last step a despiking process to eliminate massively disturbed measurements due to orbital manoeuvres etc.

Next we build pairs of $(x_e, \frac{\partial}{\partial r} V(x_e))$ from which we select in a next pre-processing step only those data which are the closest to the nodes of a Reuter grid on Ω_r as given in Definition 2.1. This provides us with an *equidistributed* set of measurements. Then we subtract a known gravitational field model for the low-frequency part, e.g. globally for degree 0–2 and locally, e.g. here over South America, up to degree 35.

3.3 Data fitting with splines

Using the Abel–Poisson kernel introduced by eq. (2) with $h = 0.95$ as a least-square adjustment or spline fitted to the data given on the satellite's orbit we extrapolate the radial derivative to a Driscoll–Healy (integration) grid on a sphere Ω_r going through the mean or median flight altitude of CHAMP (see Fig. 1). This essential step reserves the harmonicity in the data in contrast to methods of averaging, statistical selection strategies or projection methods. Due to the underlying inverse problem the linear system is usually ill-conditioned. Since the systems are in our modelling are of moderate size, e.g. (50 832 × 12 684) up to (679 200 × 12 684), we use the well-known parallel QR-algorithm PDGELS from ScaLAPACK to solve them (*cf.* Anderson *et al.* 1992; Blackford *et al.* 1997; Schwarz 1997). By using orthogonal transformations the QR algorithm does not additionally deteriorate the condition number but stabilizes the whole solution process, as it is not done by other direct or iterative methods, for example Cholesky, LU, CG etc. (*cf.* Press *et al.* 1992; Werner 1992). Running on up to 256 processors of a CRAY-T3E(1200) it takes us less than 50 min to solve such a system explained above.

3.4 Solving the inverse problem and reconstruction

By evaluating the $\mathcal{H}$-spline we can now assume that the *predicted measurements* are given on an integration grid on the sphere Ω_r. By convolving these predicted measurements as stated in Section 2.5 with the regularization scaling functions and wavelets, we are able to regularize the inverse problem and to reconstruct the potential on Ω_R. By applying a regularization in terms of multiresolution, wavelets allow us to manipulate directly the singular values of the SST operator. To define an appropriate criterion for stopping the regularization we use the standard L-curve method (for more details the reader is referred to Grafarend & Shen 2000; Kusche 2002). To be more specific, we take the recovered potential and predict the measurements shifted to the spherical integration grid on Ω_r. Since $\|\cdot\|_{\mathcal{H}(A,\Omega_R)}$ as introduced above is calculated in the spectral domain, for our local purpose we prefer here for the L-curve the $L^2(\Omega_R)$ norm. We plot the norm of the reconstructed potential (within $\text{Harm}_{25,\ldots,90}(\Omega_R)$) on the y-axis against the prediction error from this potential to the orbit data on the x-axis (*cf.* Figs 18 and 20). Locally we calculate the rooted mean square sum of the reconstructed potential values (RMS), resp. the error between the measurements and the predicted orbit values on a smaller grid, which approximates locally the $L^2(\Omega_R)$ norm. It should be remarked that the time-consuming numerical integration in the wavelet transformation is intrinsically extremely data parallel. We exploit this by using an efficient parallel implementation bases on the message passing interface (MPI) library showing the expected optimal scale speed-up (*cf.* Gropp *et al.* 1999). For a better comparison we project the solution globally on $\text{Harm}_{3,\ldots,90}(\Omega_R)$ or locally on $\text{Harm}_{36,\ldots,128}(\Omega_R)$ in order to analyse the accuracy of our method with respect to EGM96.

4 NUMERICAL RESULTS

4.1 Simulated data

4.1.1 Global reconstruction process

Preparations. To compare both the simulated models with and without noise we use for the numerical differentiation of the ephemeris in the space-fixed coordinate system the Newton-Gregory difference quotient by taking seven points into account (see eq. 1).

Let N denote the number of disturbed ephemerides, then we denoise the single Cartesian components after the differentiation. By using 1-D wavelet techniques we have to determine a threshold T for the truncation of noise-containing coefficients. By using translation-invariant hard thresholding, as suggested, for example, by Mallat (1999), Coifman & Donoho (1995) proved that the threshold $T = \tilde{\sigma}_\varepsilon \sqrt{2 \ln N}$, where $\tilde{\sigma}_\varepsilon$ denotes the standard deviation, fulfils certain optimality criteria: the threshold should be chosen just above the maximum level of the noise but should also not be too large so that we do not set too many coefficients to zero. Assuming that we consider a vector of N Gaussian random variables of variance σ^2, one can prove that the maximum amplitude of the noise has a very high probability of being just below T. That the threshold increases with N seems to be counterintuitive. This is due to the tail of the Gaussian distribution, which creates larger and larger amplitude noise coefficients when the sample rate increases. The threshold is not optimal, and in general a lower threshold reduces the risk. However, one can prove that when $N \to \infty$, the optimal value of T grows like $\tilde{\sigma}_\varepsilon \sqrt{2 \ln N}$.

Further, for a global data selection we used two of the above introduced Reuter grids for applying the selection algorithm. The first one consists of 91 56 points, and is used for the spherical spline approach resulting in a linear system of 91 56 unknowns. The second one is of size 15 132 and provides enough data for a reliable least-squares adjustment. Using the first grid as the *park grid* for the kernels we obtain an overdetermined linear system of size 15 132 × 91 56.

Regularization of the inverse problem. For the evaluation of the convolution with the Tikhonov scaling function we use a Driscoll–Healy grid with about 250 000 integration points. For the

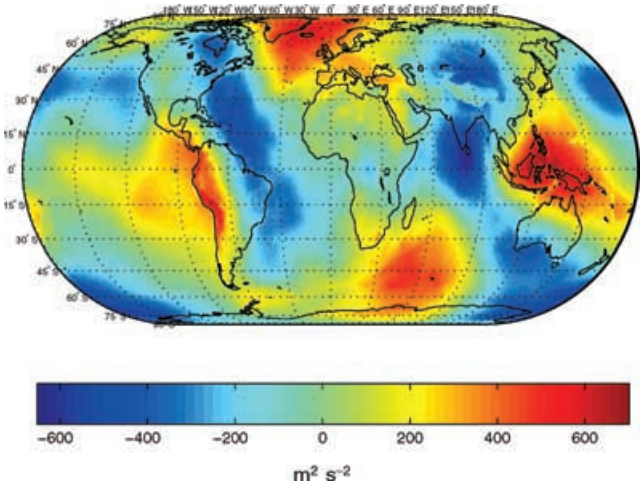

Figure 3. Disturbing potential generated by EGM96 from degree/order 3 up to 200 on Ω_R.

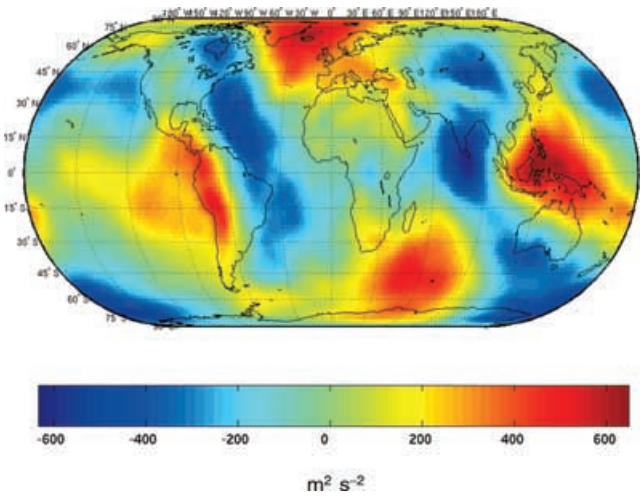

Figure 4. Recovered potential from the simulated ephemerides within degree/order 3 up to 90 on Ω_R.

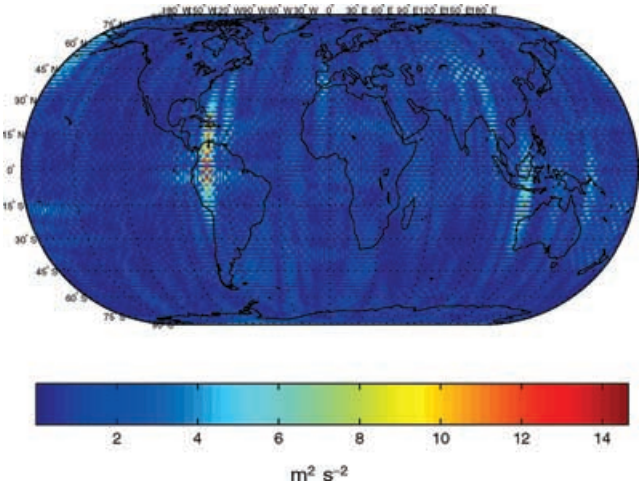

Figure 5. Absolute error in the reconstructed potential from noise-free data within degree 3 up to 90 on Ω_R.

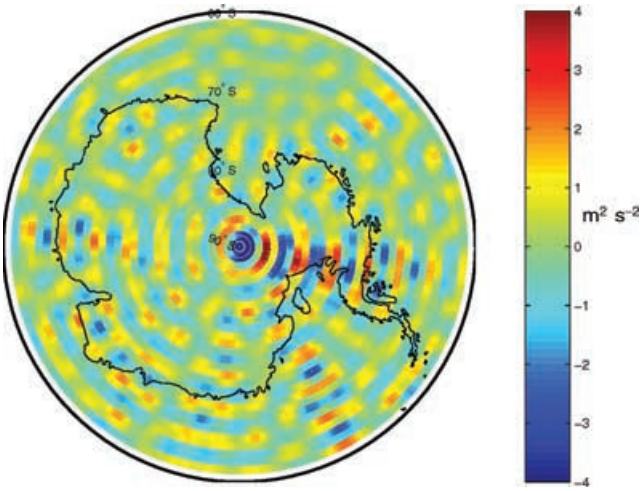

Figure 6. Difference in the reconstruction at the South Pole from noise-free data with respect to EGM96 within degree 3 up to 90 on Ω_R.

reconstruction grid at the Earth's surface for considering a global error analysis we use an equidistant ϕ–θ grid with 180 samples in ϕ direction and 90 in θ.

First we consider the noise-free case to determine the numerical accuracy of our method. However, one should note that we act with non-bandlimited functions on band-limited data, which is not the case in practice. By combining the spline interpolation and wavelet regularization we find based on the L-curve method a good regularization parameter for the Tikhonov regularization scaling function at $\gamma_J = 0.000\,001$. This results in a high-quality recovered potential as Figs 3 to 6 show, where the mean absolute error computed on an equiangular 2° grid is at 1.03 m^2 s^{-2}, and the median absolute error is at 0.61 m^2 s^{-2}.

These results could not be improved by combining the least-squares adjustment and wavelet regularization. The mean absolute error is 1.03 m^2 s^{-2}, and the median absolute error is 0.73 m^2 s^{-2}. Even in polar regions, where one would expect bigger problems due to the polar gap, both methods give reliable results (see the combination of the least-squares adjustment and regularization wavelets at the South Pole in Fig. 6).

More interesting is the analysis of the recovered potential from noisy ephemerides. Our numerical differentiation and de-noising with TI-thresholding yields a mean absolute error of 5.34×10^{-6} m^2 s^{-2} in the radial derivative on Ω_r. Then the least-squares adjustment proves its superiority against the interpolating spline technique as the following error plots show. Finding a best approximation for $\gamma = 0.1$ the combination with the interpolating spline and the wavelet regularization results in a mean absolute error of 17.22 m^2 s^{-2} and a median absolute error of 15.51 m^2 s^{-2}.

It can easily be seen from Fig. 7 that the spline yields larger errors in regions where the underlying gravitational potential is very large. However, the combination of the least-squares adjustment spline and the regularization Tikhonov scaling functions improves the mean absolute error to 9.23 m^2 s^{-2} and the median absolute error to 6.23 m^2 s^{-2}, *cf.* Fig. 8.
These results show that the least-squares adjustment method combined with Tikhonov wavelet regularization is an appropriate method for global data modelling.

However, we would like to explore whether we can achieve even better local models. In what follows we try to recover the gravitational potential up to a resolution of spherical harmonic degree

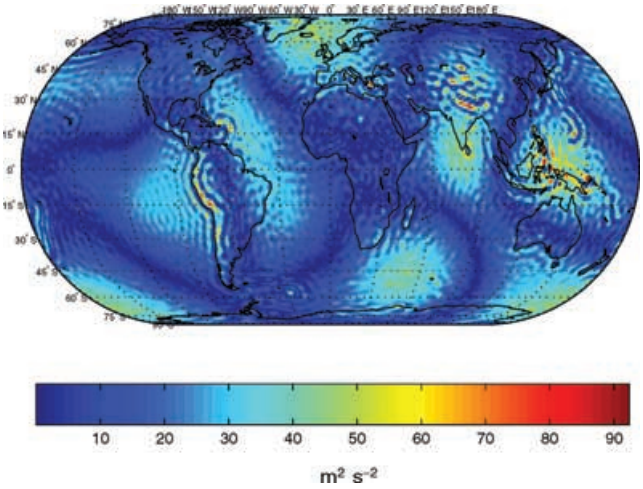

Figure 7. Combined interpolating spline and regularization wavelets on noisy data. Error in the reconstructed potential on Ω_R from degree 3 up to 90.

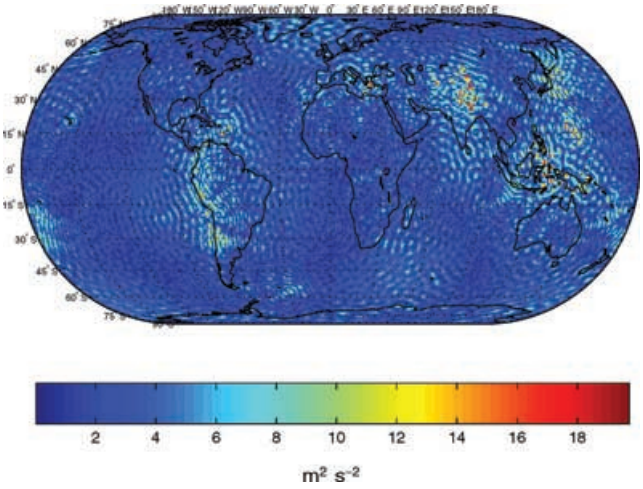

Figure 8. Combined least-squares adjustment and regularization wavelets on noisy data. Error in the reconstructed potential on Ω_R from degree 3 up to 90.

128 over South America. Therefore, we subtract from the evaluated orbital radial derivative a 'known' model up to degree 35, for example provided by EGM96. This protects us from effects induced by the support of spherical harmonics with a *wavelength* larger than 1100 km in our reconstruction area. Additionally we project the reconstructed model on to $\mathrm{Harm}_{36,\ldots,128}(\Omega_R)$ to analyse its quality by comparing it with a potential $\widetilde{V}$ generated by EGM96 from degree 36–128. In the following we stick to the realistic case of recovering the gravitational potential from locally given noisy ephemerides. Therefore, we focus on the connection of the least-squares adjustment and wavelets.

4.1.2 Local reconstruction process

Since the Tikhonov scaling functions and wavelets are strongly localizing on Ω_R the influence of each in the reconstruction convolution depends only on a small local cap. Thus, we can think of a *numerically, locally compact support*. This is the reason why we are able to compute a reconstruction of the gravitational potential in a desired area. We have to first determine a local data window providing the data, a corresponding part of a Reuter grid for the selection process, a local integration grid, a local grid for the reconstruction and at least a small orbital prediction grid for the L-curve method.

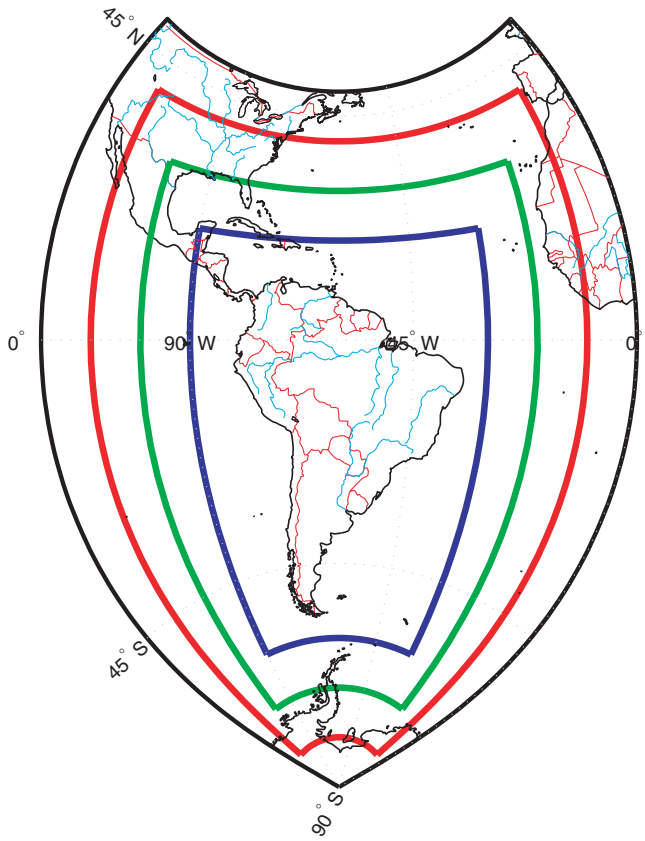

Figure 9. The Reuter selected satellite data are assumed to be given in the red marked window, while the green integration window is a fraction of a fine Driscoll–Healy grid. The local reconstruction over South America is done in the blue reconstruction window on an equidistant ϕ–θ grid.

In the following example we zoomed into South America trying to improve the resolution accuracy.

Therefore, we set the data window to $[-80^\circ, 40^\circ] \times [-110^\circ, -10^\circ]$ considering 19 256 (noisy) observations, while the *park grid* for the least-squares adjustment is of the same size as the data window and contains 4063 points of a Reuter grid. The integration window is smaller and set to $[-70^\circ, 30^\circ] \times [-100^\circ, -20^\circ]$ containing 28 112 integration points of a corresponding Driscoll–Healy grid. The reconstruction window with 32400 points is given by $[-60^\circ, 20^\circ] \times [-90^\circ, -30^\circ]$ (see Fig. 9). The prediction grid is again 10° smaller on each side and a subset from the orbital integration grid.

By viewing only the reconstructions of highest scale in the global data modelling of the simulated CHAMP data we omitted a technical feature of wavelet analysis which will be explained now in more detail. It turns out that the multiresolution analysis (MRA) provides us an excellent tool for detecting certain features of the high-frequency phenomena of the locally recovered gravitational potential. Additionally, we are able to analyse how the locally given data materially influences the quality of the reconstruction. From this we can deduce limits of the discussed method of combining the least-squares adjustment and the wavelet regularization, which will help improve this strategy in our future research.

For analysing the recovered potential from degree 36 up to 128, we create an MRA generated by regularization scaling functions.

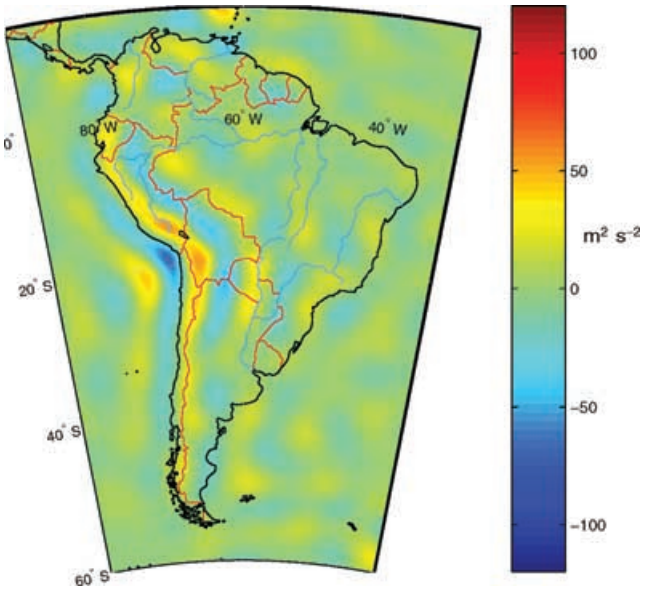

Figure 10. Approximation of $\widetilde{V}$ in the scale space of level 0, with $\gamma_0 = 2.0$.

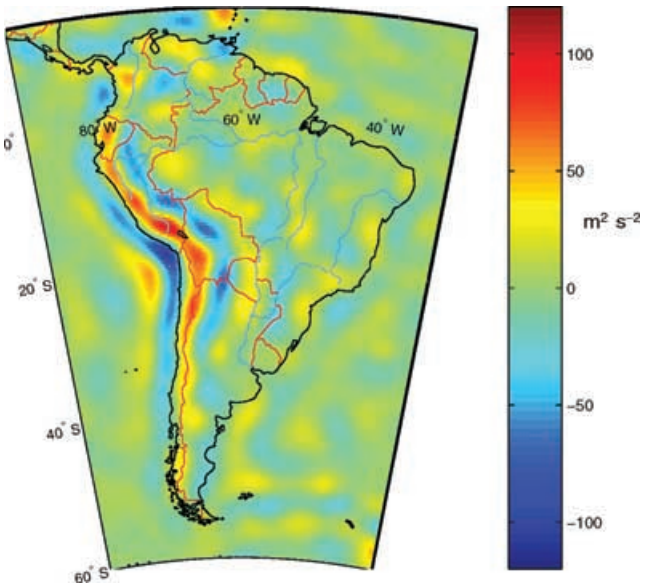

Figure 12. Approximation of $\widetilde{V}$ in the scale space of level 1, with $\gamma_1 = 0.2$.

This MRA enables us to analyse the regional signal content by considering an increasing sequence of low-pass approximations, the so-called *scale spaces*. The difference between two such consecutive scale spaces can be characterized by some added detailed structure generated by the wavelet space in between. Therefore these spaces are called *detail spaces*, and if we track the (energy) content of these detail spaces we are able to develop stopping criteria to balance the error induced by recovering too noisy high-frequency phenomena.

To be specific for this example, we define a strict monotonically decreasing sequence γ_j, $j \in \mathbb{N}_0$, with $\lim_{j\to\infty}\gamma_j = 0$. We consider only the first elements of this sequence given by γ_j, $j = 0, 1, 2, 3$, where γ_0 is the Tikhonov regularization parameter of the lowest scale, and γ_3 the regularization parameter of the highest scale. More explicitly,

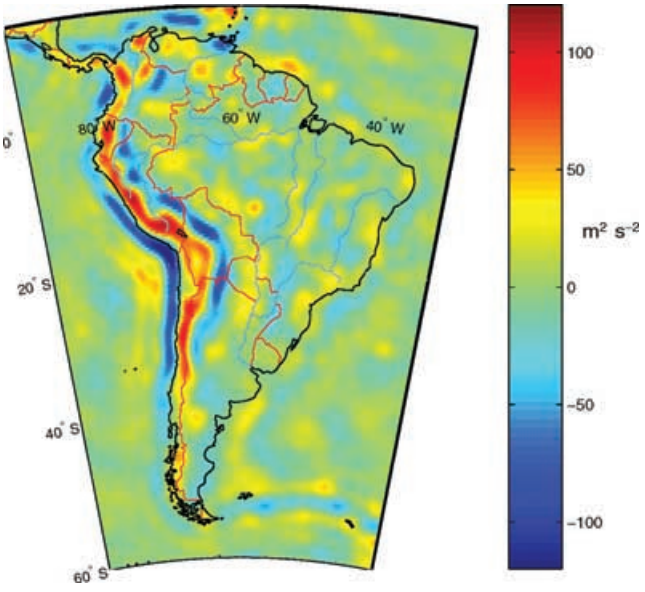

Figure 11. Potential $\widetilde{V}$ generated by EGM96 36–128.

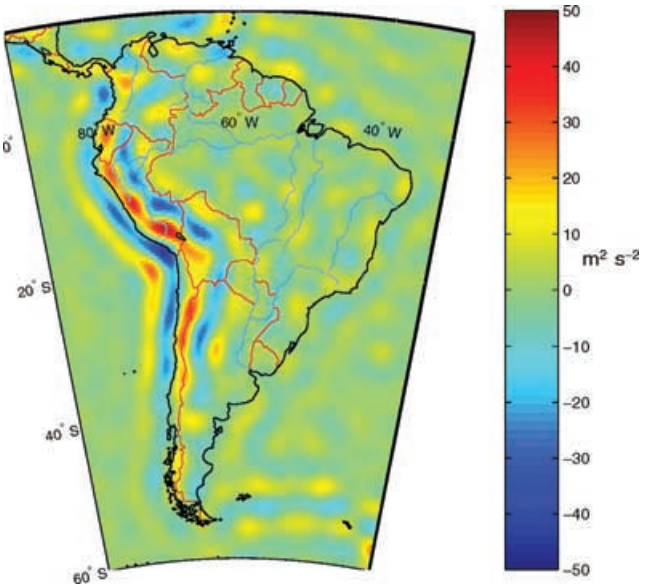

Figure 13. Approximation of $\widetilde{V}$ in the detail space of level 0.

$$\gamma_0 = 2.000, \quad \gamma_1 = 0.200,$$
$$\gamma_2 = 0.050, \quad \gamma_3 = 0.005.$$

We start with the low-frequency approximation given by $\gamma_0 = 2.0$ in Fig. 10 having a mean absolute error of 8.4586 $m^2\ s^{-2}$ to the potential generated by EGM96 from degree 36 up to 128 as illustrated in Fig. 11.

As we can see in Fig. 10 only the most significant structures are visible, for instance the deep ocean trench off the west coast of South America. Adding the structures appearing in the detail space of level 0, see Fig. 13, we get the scale approximation of level 1, yielding a mean absolute error of 5.925 $m^2\ s^{-2}$ (*cf.* Fig. 12).

A further decrease of γ_j adding the details of Fig. 15, yields with the approximation in level $j = 2$ a mean absolute error of 4.909 $m^2\ s^{-2}$ (*cf.* Fig. 14).

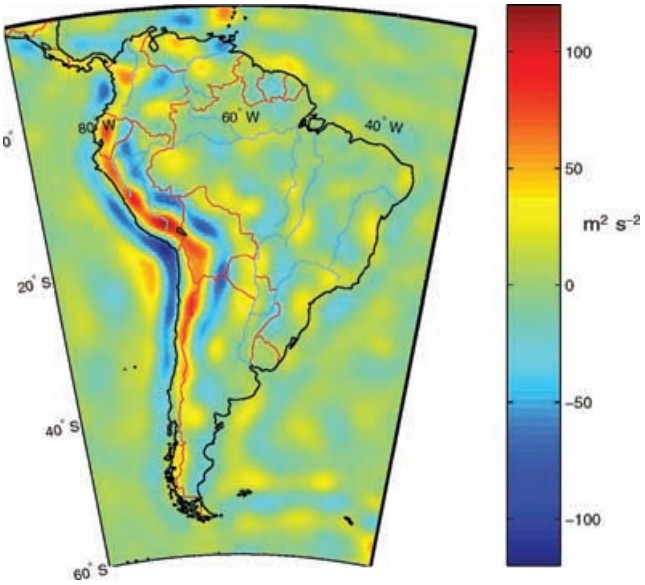

Figure 14. Approximation of $\widetilde{V}$ in the scale space of level 2, with $\gamma_2 = 0.05$.

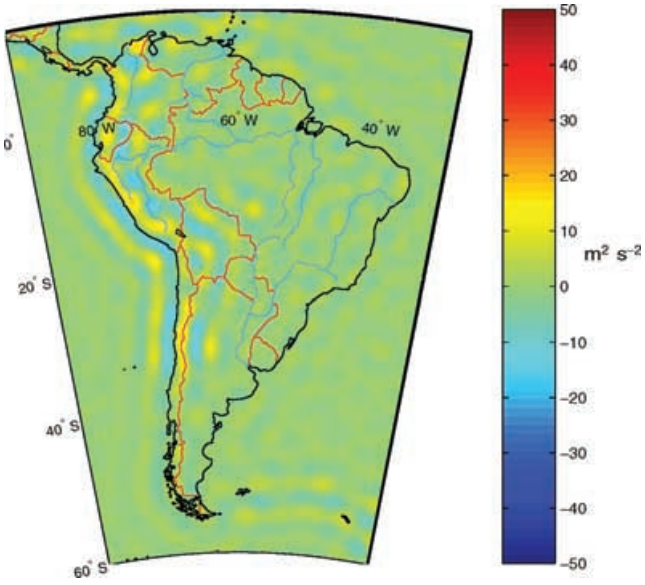

Figure 15. Approximation of $\widetilde{V}$ in the detail space of level 1.

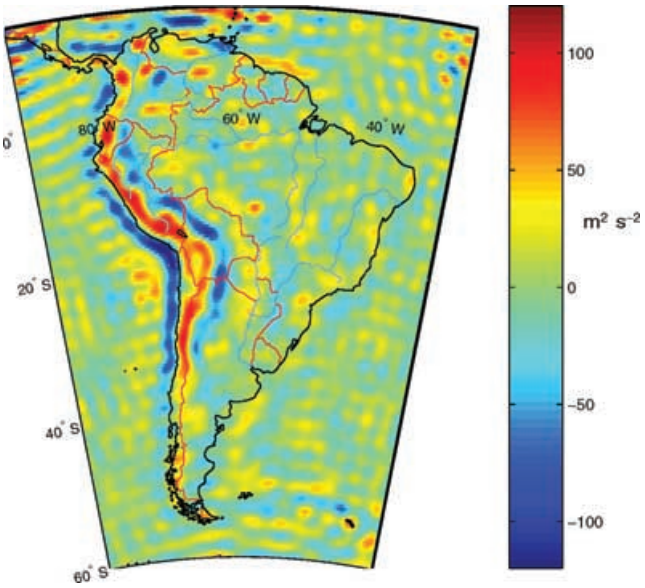

Figure 16. Approximation of $\widetilde{V}$ in the scale space of level 3, with $\gamma_3 = 0.005$.

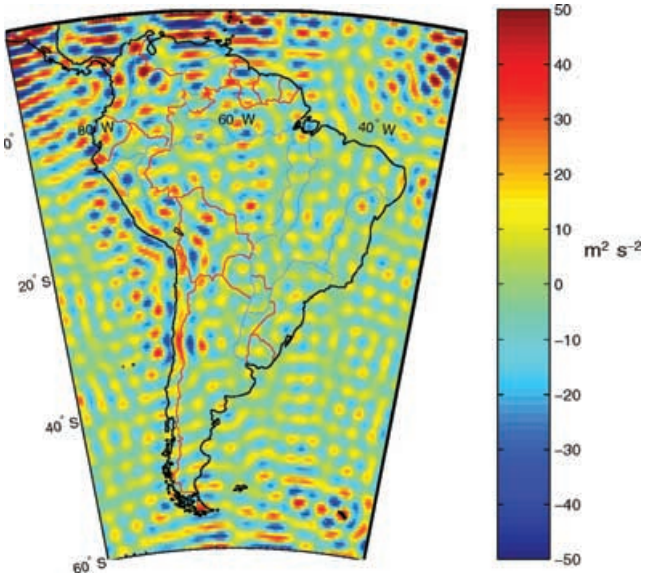

Figure 17. Approximation of $\widetilde{V}$ in the detail space of level 2.

The sequence of γ_j was chosen here so as to demonstrate a common problem in regularization concepts. As we can see in Figs 16 and 17 the approximation error increases with a further decrease in the γ_j values. Thus, we have to take care with real data to achieve reliable results.

The detailed structure obtained from level 2 adds artefacts which destroy the quite good approximation in the scale approximation of level 2.

The parameter sequence γ_i, $i = 0, 1, 2, 3$, is here motivated by the shape of the L-curve in Fig. 18 which yields us almost optimal regularization parameters, i.e. in simulations one can determine the optimal regularization parameters by comparing the recovered potential with the input model. For the prediction error we reconstruct from the locally regularized potential within band 36–128 the same frequency band for the data having been shifted to the integration grid in orbital height. They have also been filtered for the same frequency band.

It is good to see that with decreasing γ_j we encounter instabilities in the norm of the potential. With further increasing $\gamma_j \gg 2$ the prediction error increases. As Fig. 14 shows the value of $\gamma_j = 0.05$ is almost optimal. Therefore, we may assume that the (heuristic) L-curve method is an appropriate tool in our whole concept to find good regularization parameters for real data.

4.1.3 Conclusion

As we have seen, the combination of a least-squares adjustment, Tikhonov regularization wavelets and the L-curve method gives good results, especially on noisy data, globally as well as locally. This leads us to the opinion that the concept presented here is appropriate for solving the SST problem and, thus, for the evaluation of real CHAMP data.

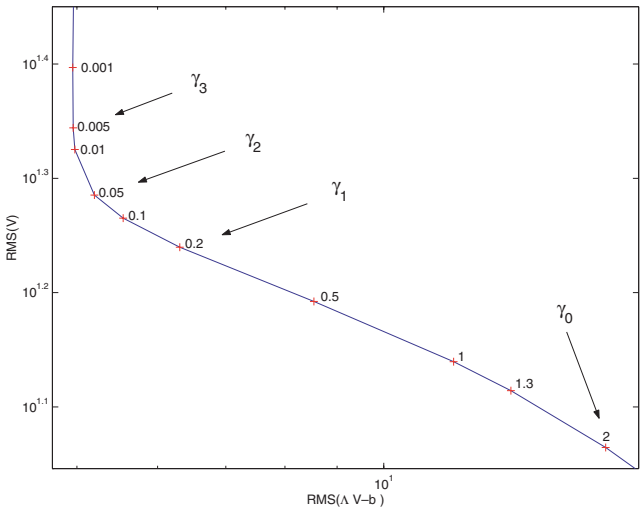

Figure 18. Local L-curve for simulated ephemeris over South America, degree 36–128.

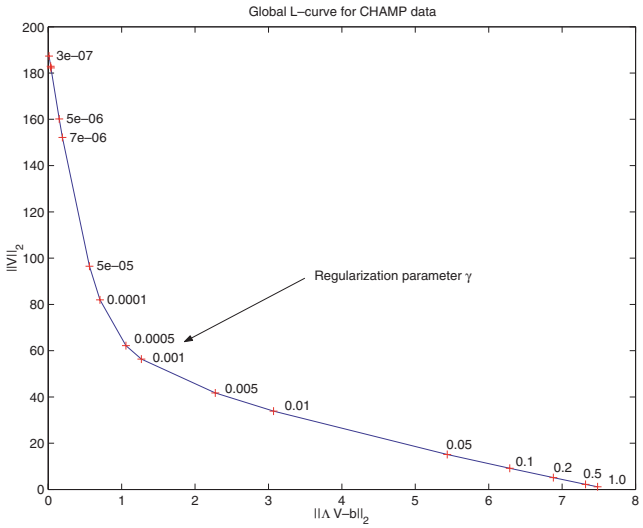

Figure 19. Global L-curve for CHAMP data within $\mathrm{Harm}_{25,\ldots,90}(\Omega_R)$.

4.2 Real CHAMP data analysis

4.2.1 Global CHAMP model

The Delft Institute for Earth-oriented Space Research (DEOS) provided us with pre-processed CHAMP orbits obtained from so-called post-processed science orbits (PSO) of the GeoForschungsZentrum Potsdam (GFZ). These data contain measurements taken in the first 5 months of 2002. They have been corrected for accelerometer data, precession and nutation, and gravitational effects induced by third bodies. Thereby they follow, with some modifications, the ideas of Jekeli's energy balance method see Kusche & van Loon (2003) and Jekeli (1999). Thus, by subtracting an EGM96 potential up to degree 24 they provide anomalous potential values along the track. Depending on the PSO input data the resolved Earth gravitational field models are not completely independent of other existing models, i.e. one expects an EIGEN-2 related model (Schwintzer 2003).

Although these data do not directly lead to gradient vectors or radial derivatives as discussed so far, we are able to use these real data with obvious slight modifications of our modelling approach, i.e. the symbol of the pseudodifferential operator Λ has to be changed to $(\frac{R}{r})^{n+1}$. As a consequence, we are also able to demonstrate the strength of our spline-based wavelet concept on the provided 'CHAMP data set' (see Freeden 1999).

By using cubic approximating splines, as discussed in Engeln-Müllges & Reutter (1988), we corrected obvious trends in the data which are induced by accelerometer drifts. The remaining noise is compensated by fitting a least-squares adjustment spline with 12 684 points on the park grid and 679 200 measurements to compensate for this. The shape of the 'L-curve' in Fig. 19 shows the classical 'L-shape': the norm of the reconstructed potential is very sensitive to small variations of the regularization parameter for small $\gamma \approx 0$. For larger values of γ the prediction error increases while the norm of the potential further decreases. Thus, we deduce here that $\gamma = 0.001$ is a good compromise.

First we reconstruct a global solution called SWITCH-03 for the higher-frequency parts (degree 25–90) and compare it with EGM96 (Lemoine *et al.* 1998), UCPH2002_02_0.5 (Stenseng & Tscherning 2003), EIGEN-1s (Schwintzer 2002) and EIGEN-2 (Reigber *et al.* 2002) within $\mathrm{Harm}_{25,\ldots,90}(\Omega_R)$, see Figs 20 and 21.

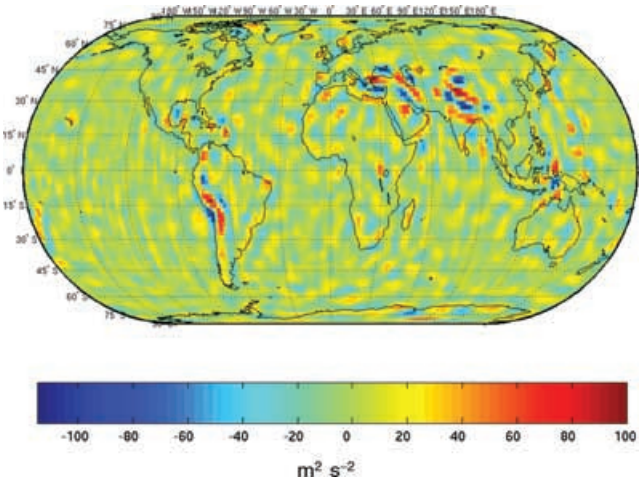

Figure 20. SWITCH-03 potential within $\mathrm{Harm}_{25,\ldots,90}(\Omega_R)$.

As, for example, Fig. 24 shows that only very high-frequency parts contribute to the differences between SWITCH-03 and EIGEN-2, e.g. in the Andes we have the largest differences from EIGEN-2 with about ± 56 m^2 s^{-2}. Table 1 indicates the differences in the globally recovered potential referring to the illustrations in Figs 21–24.

4.2.2 Local CHAMP data analysis

The differences in the high-frequency part of the SWITCH-03 model, especially in the Andes, now have to be further investigated. Thus, we analyse the region around the Andes and try to improve our global results locally.

Therefore, we consider the same windows as in the simulations and use the 'optimal' regularization parameter given by the *local L-curve* from Fig. 25. This L-curve differs slightly from that in the global data modelling since we focus only on data material given in this specific region. The key advantage of our method is obvious: We can deduce from the L-curve given by Fig. 25 that the globally obtained regularization parameter is by means too large for this specific region, and thus high-frequency phenomena are smoothed away. Beyond this, the local L-curve states that $\gamma = 0.0001$ is a

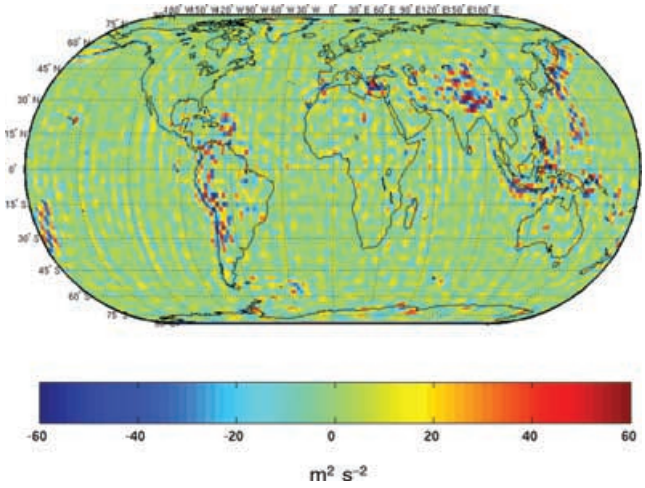

Figure 21. Difference between the SWITCH-03 potential and EGM96 in $\mathrm{Harm}_{25,\ldots,90}(\Omega_R)$.

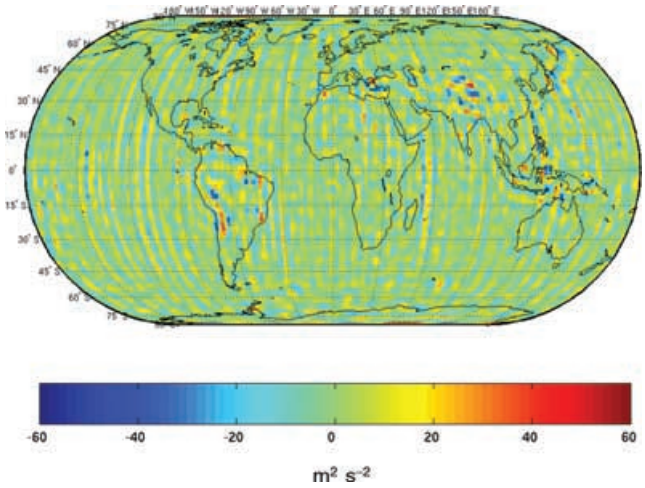

Figure 22. Difference between the SWITCH-03 potential and UCPH2002_02_0.5 in $\mathrm{Harm}_{25,\ldots,90}(\Omega_R)$.

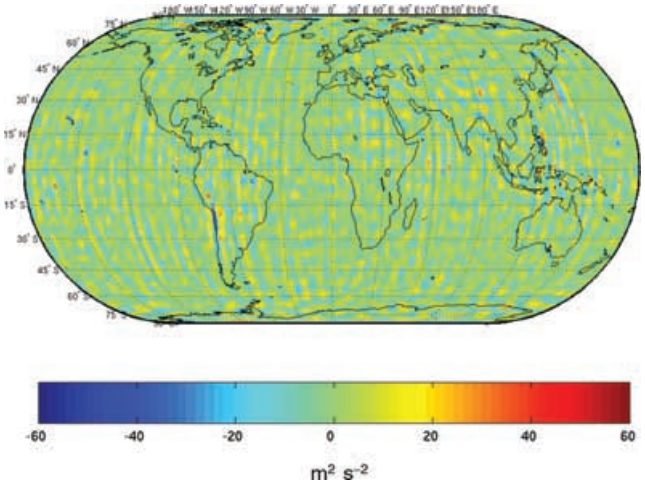

Figure 23. Difference between the SWITCH-03 potential and EIGEN-1s in $\mathrm{Harm}_{25,\ldots,90}(\Omega_R)$.

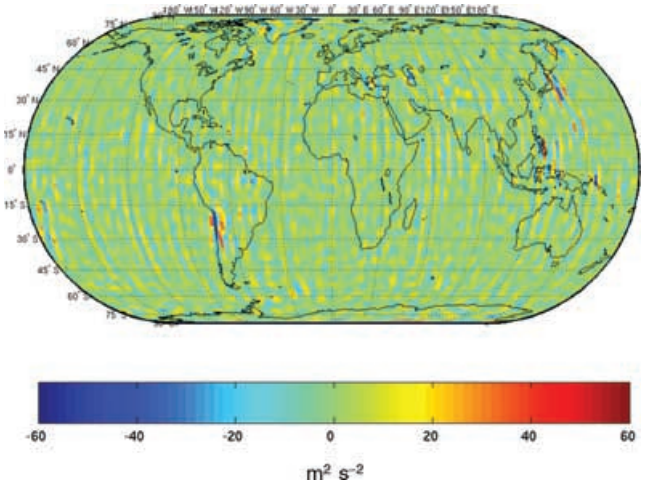

Figure 24. Difference between the SWITCH-03 potential and EIGEN-2 in $\mathrm{Harm}_{25,\ldots,90}(\Omega_R)$.

good choice for this region. It turns out that we are able to improve our model locally, e.g. more details are visible (see Fig. 26). To be specific, the peak differences between EIGEN-1s and EIGEN-2 could be significantly decreased from *ca.* 60 $\mathrm{m^2\ s^{-2}}$ to *ca.* 20 $\mathrm{m^2\ s^{-2}}$ or even less (see Figs 29 and 30). The remaining differences are small but still evident and can be located at the highest frequency parts in the Andes and the maximum is at 23.06 $\mathrm{m^2\ s^{-2}}$. Nevertheless, in a composition of the global and the local model the globally computed median and mean absolute difference to the EIGEN-2 model reduces to 3.41 $\mathrm{m^2\ s^{-2}}$, resp. 4.82 $\mathrm{m^2\ s^{-2}}$, which improves the results stated in Table 1. It should be remarked that the same procedure may also be applied to other regions, e.g. Tibet.

It should be the aim content of future work to further investigate the visible tracks in the difference plots, and the errors that might be introduced trackwise by some 'bad days' of the accelerometer.

The reader should note that due to the much larger differences from EGM96 the colour bar for the difference plot in Fig. 27 is two times larger than that for EIGEN-1s, EIGEN-2 and UCPH2002_02_0.5 (see Figs 28–30), where the colour bar is fixed to the same size.

5 CONCLUSION

These results show that our spline-based wavelet method is able to suitably handle the given data material and additionally improve existing results leading to a satellite-only gravitational field model SWITCH-03 based on wavelets. Further we have achieved a method which is very appropriate for real data applications since our programs are fully parallelized using the message passing interface (MPI) (see, e.g. Gropp *et al.* 1999). By exploiting the evident data parallelism in the numerical integration routines it yields a nearly optimal scale speed-up on parallel machines.

ACKNOWLEDGMENTS

The authors are grateful to Prof. Dr J. Kusche from DEOS for his great support and modified CHAMP data material, that he obtained from PSO orbits and accelerometry data kindly provided by GFZ Potsdam. Further we are obliged to the Research Centre in Jülich, the ITWM-Fraunhofer Institute, and the Regionales Hochschulrechenzentrum in Kaiserslautern for use of their computational equipment, e.g. Cray-T3E(1200), IBM RS/6000 44P Model 270 and several Linux-Clusters.

Table 1. Globally computed potential differences in $m^2\ s^{-2}$ between SWITCH-03 and the considered models.

	EGM96	UCPH_2002_0.5	EIGEN-1s	EIGEN-2
Median absolute difference	4.531	4.956	3.695	3.564
Mean absolute difference	6.629	6.932	5.296	5.270

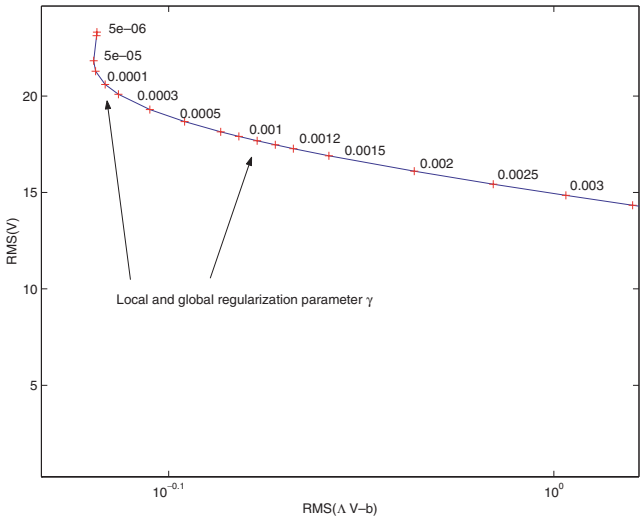

Figure 25. Local L-curve for CHAMP data over South America in $\mathrm{Harm}_{25,\ldots,90}(\Omega_R)$.

In particular, the authors are indebted to Dr P. Schwintzer, GFZ Potsdam, for his advice and valuable comments concerning the data models UCPH2002_02_0.5, EIGEN-1s, EIGEN-2 and SWITCH-03 during a visit to Kaiserslautern.

REFERENCES

Ahlberg, J.H., Nilson, E.N. & Walsh, J.L., 1967. *The Theory of Splines and Their Application.* Academic Press, New York.

Anderson, E. *et al.,* 1992. *LAPACK Users' Guide, Release 1.0*, SIAM, Philadelphia, PA.

Austen, G. & Reubelt, T., 2000. Spatial gravity field analysis using semi-continuous ephemerides of low-orbiting GPS-tracked satellites of type CHAMP, GRACE and GOCE, *Diplomarbeit*, Geodätisches Institut, Universität Stuttgart.

Balmino, G. & Barriot, J.P., 1989. Study on precise gravity field determination methods and mission requirements, *Final Report, ESA 7521/87/F/FL, Workpackage 221: Revision of Numerical Techniques*,

Barlier, F. *et al.,* 2000. A new global Earth's gravity field model from satellite orbit perturbations: GRIM5-S1, *Geophys. Res. Lett.,* **27,** 3611–3614.

Blackford, L.S. *et al.,* 1997. *ScaLAPACK Users' Guide*, SIAM. Philadelphia, PA.

Coifman, R.R. & Donoho, D.L., 1995. *Translation-Invariant De-Noising*, Yale University and Stanford University, Proceedings of the 15th French-Belgian meeting of statisticians, New York, Springer.

Daubechies, I., 1988. Orthonormal bases of compactly supported wavelets, *Comm. Pure appl. Math.,* **41,** 909–996.

Driscoll, J.R. & Healy, D.M., 1994. Computing Fourier transforms and convolutions on the 2-sphere, *Adv. Appl. Math.,* **15,** 202–250.

Engeln-Müllges, G. & Reutter, F., 1988. *Numerik-Algorithmen mit ANSI C-Programmen*, BI-Wiss. Verlag, Mannheim.

Fengler, M.J., 2002. Multiscale modeling of the Earth's gravitational potential from discrete noisy CHAMP ephemerides, *Diploma thesis,* Geomathematics Group, Department of Mathematics, University of Kaiserslautern.

Freeden, W., 1981a. On approximation by harmonic splines, *Manuscr. Geod.,* **6,** 193–244.

Freeden, W., 1981b. On spherical spline interpolation and approximation, *Math. Methods Appl. Sci.,* **3,** 551–575.

Freeden, W., 1983. Least square approximation by linear combinations of (multi)poles, *Department of Geodetic Science and Surveying Report 344*,

Freeden, W., 1999. *Multiscale Modelling of Spaceborne Geodata*, Teubner Verlag, Stuttgart.

Freeden, W. & Hesse K., 2002. Spline modelling of geostrophic flow: theoretical and algorithmic aspects, *Report 250*, Geomathematics Group, University of Kaiserslautern.

Freeden, W. & Michel, V., 1999. Constructive approximation and numerical methods in geodetic research today—an attempt at a categorization based on an uncertainty principle, *J. Geodesy.,* **73,** 452–465.

Freeden, W., Schreiner, M. & Franke, R., 1997. A survey on spherical spline approximation, *Surv. Math. Ind.,* **7,** 29–85.

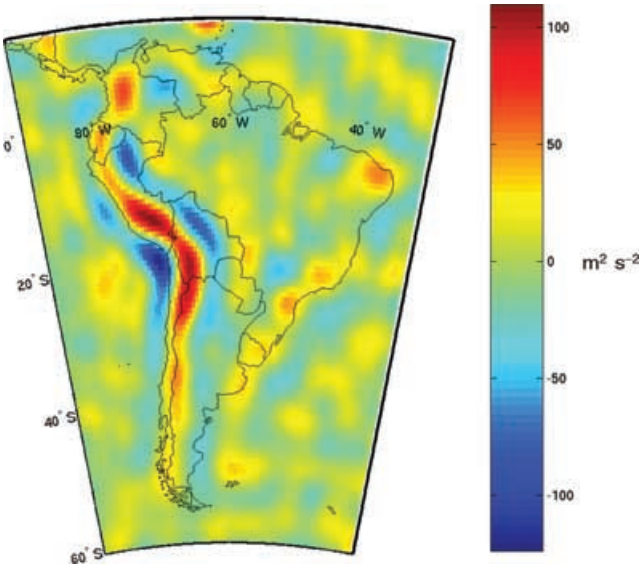

Figure 26. Locally improved SWITCH-03 Potential in $\mathrm{Harm}_{25,\ldots,90}(\Omega_R)$.

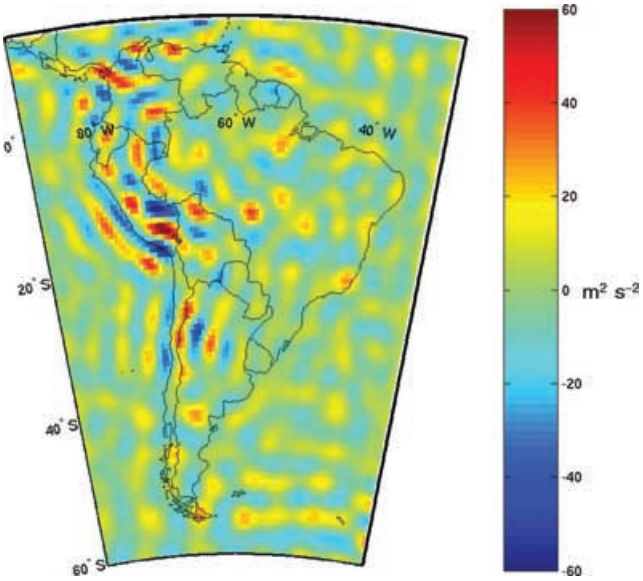

Figure 27. Local difference between SWITCH-03 and EGM96 in $\mathrm{Harm}_{25,\ldots,90}(\Omega_R)$.

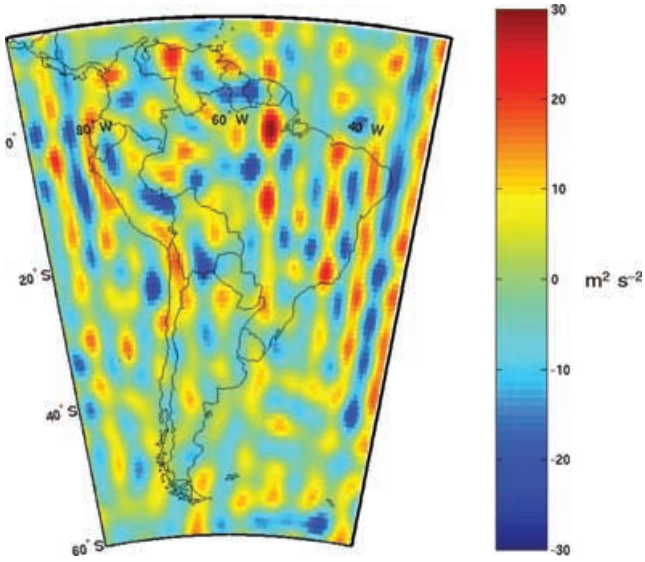

Figure 28. Local difference between SWITCH-03 and UCPH2002_02_0.5 in $\mathrm{Harm}_{25,\ldots,90}(\Omega_R)$.

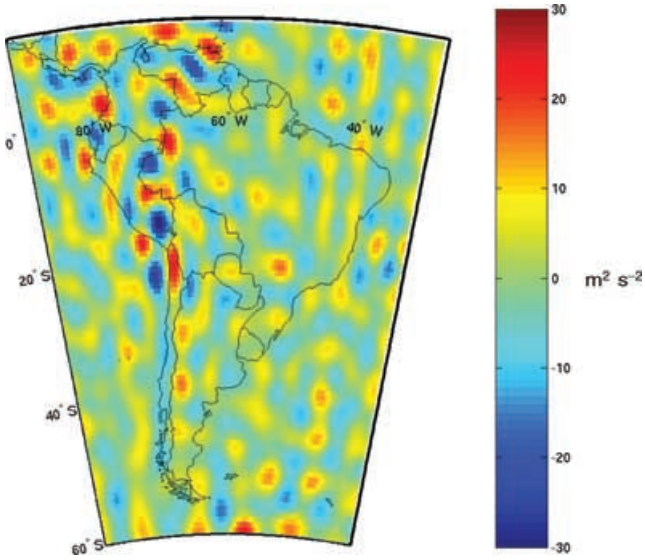

Figure 29. Local difference between SWITCH-03 and EIGEN-1s in $\mathrm{Harm}_{25,\ldots,90}(\Omega_R)$.

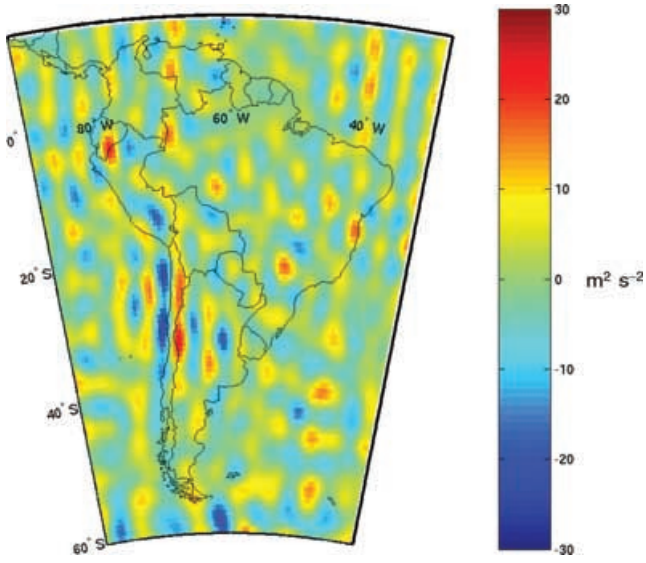

Figure 30. Local difference between SWITCH-03 and EIGEN-2 in $\mathrm{Harm}_{25,\ldots,90}(\Omega_R)$.

Freeden, W., Gervens, T. & Schreiner, M., 1998. *Constructive Approximation on the Sphere (with Applications to Geomathematics),* Clarendon Press, Oxford.

Freeden, W., Glockner, O. & Thalhammer, M., 1999. Multiscale gravitational field recovery from GPS-satellite-to-satellite tracking, *Stud. Geophys. Geodaetica,* **43,** 229–264.

Freeden, W., Michel, V. & Nutz, H., 2002. Satellite-to-satellite tracking and satellite gravity gradiometry (advanced techniques for high-resolution geopotential field determination), *J. Eng. Math.,* **43,** 19–56.

Glockner, O., 2001. On numerical aspects of gravitational field modelling from SST and SGG by harmonic splines and wavelets, *PhD thesis*, Geomathematics Group, University of Kaiserslautern, Shaker Verlag, Aachen.

Grafarend, E. & Shen, Y.Z., 2000. *Study and simulation of recovering the gravitational potential model from the ephemerides of CHAMP,* preprint.

Green, P.J. & Silvermann B.W., 1994. *Nonparametric Regression and Generalized Linear Models,* Monographs on Statistics and Applied Probability 58. Chapman & Hall, London.

Gutting, M., 2002. Multiscale gravitational field modelling from oblique derivatives, *Diploma thesis,* Geomathematics Group, Department of Mathematics, University of Kaiserslautern.

Gropp, W., Lusk, E. & Skjellum, A., 1999. *Using MPI—Portable Parallel Programming with the Message-Passing Interface,* 2nd edn, MIT Press, Cambridge, MA.

Han, S.-C., Jekeli, C. & Shum C.K., 2002. Efficient gravity field recovery using *in situ* disturbing potential observables from CHAMP, *Geophys. Res. Lett.,* **29,** 10.1029/2002GL015180.

Jekeli C., 1999. The determination of gravitational potential differences from satellite-to-satellite tracking, *Cel. Mech. Dyn. Astron.,* **75,** 85–101.

Kellogg, O.D., 1929. *Foundations in Potential Theory,* Frederick Ungar Publishing Company.

Kusche, J., 2002. Inverse Probleme bei der Gravitationsfeldbestimmung mittels SST- und SGG-Satellitenmissionen, *Habilitationsschrift,* Fachgebiet Geodäsie, Friedrich-Wilhelms-Universität, Bonn.

Kusche, J. & van Loon J., 2003. Statistical assessment of CHAMP data and models using the energy balance approach, *2nd CHAMP Science Meeting at the GeoForschungsZentrum Potsdam (GFZ)*.

Lawton, W.M., 1991. Necessary and sufficient conditions for constructing orthonormal wavelet bases, *J. Math. Phys.,* **32,** 1, 57–61.

Lemoine, F.G. *et al*., 1998. The development of the joint NASA GSFC and NIMA geopotential model EGM96, *NASA/TP-1998-206861,* NASA Goddard Space Flight Center, Greenbelt, MD.

Mallat, S., 1999. *A Wavelettour of Signal Processing,* Academic Press, New York.

Michel, D., 2001. On the combination of harmonic splines and fast multipole methods for CHAMP data modelling, *Diploma thesis,* Geomathematics Group, Department of Mathematics, University of Kaiserslautern.

Moritz, H., 1980. *Advanced Physical Geodesy,* H. Wichmann Verlag, Karlsruhe.

Müller, C., 1966. *Spherical Harmonics,* Springer Lecture Notes in Mathematics 17, Springer, Berlin.

Müller C., 1969. *Die Grundlehren der Mathematischen Wissenschaften in Einzeldarstellungen,* [Foundation of the Mathematical Theory of Electromagnetic Waves], Springer, Berlin.

Press, W.H., Teukolsky, S.A., Vetterling, W.T. & Flannery, B.P., 1992. *Numerical Recipes in C, The Art of Scientific Computing,* Cambridge University press, Cambridge.

Reigber, C.H., Bock, R., Förste, C., Grunwaldt, L., Jakowski, N., Lühr, H., Schwintzer, P. & Tilgner, C., 1996. CHAMP—phase B, executive summary, *Scientific Technical Report STR96/13,* GFZ, Potsdam.

Reigber, C.H. *et al.,* 2002. A high quality global gravity field model from CHAMP GPS tracking data and accelerometry (EIGEN-1S), *Geophys. Res. Lett.,* **29**(14), 10.1029/2002GL015064.

Reigber, C.H. *et al.,* 2002. The CHAMP-only EIGEN-2 Earth gravity field model, *Adv. Space Res.,* submitted.

Reubelt, T., Austen, G. & Grafarend, E. W., 2003. Harmonic analysis of the Earth's gravitational field by means of semi-continuous ephemeris of a low Earth orbiting (LEO) GPS-tracked satellite—case study CHAMP, *J. Geodesy,* **77,** 257–278.

Reuter, R., 1982. Über Integralformeln der Einheitssphäre und harmonische Splinefunktionen, Geodetic Institute, Rheinisch' Westfälische technische Hochschule, Aachen.

Schwarz, H. R., 1997. *Numerische Mathematik*, Teubner, Stuttgart.

Schwintzer, P., 2002. EIGEN-1S: first Earth gravity field model including CHAMP tracking data, http://op.gfz-potsdam.de/champ/results/index_RESULTS.html.

Schwintzer, P., 2003. Private communication.

Stenseng, L. & Tscherning, C.C., 2003. SAGRADA—SAtellite GRAvity Data Analysis, http://www.gfy.ku.dk/stenseng/sagrada.php.

Stockis, J.-P., 2001. On time series, *Lecture Notes,* Department of Statistics, University of Kaiserslautern.

Sweldens, W. & Jawerth, B., 1994. An overview of wavelet based multiresolution analyses, *SIAM Rev.,* **36**(3), 377–412.

van de Geijn, R. A., 1997. *Using PLAPACK*, MIT Press, Cambridge, MA.

Werner, J., 1992. *Numerische Mathematik I,* Vieweg Studium Verlag, Braunschweig.